4.3. Measurements of the diameter of complexes

Polymer and siRNA complexes were prepared by incubating both the siRNA and the polymer in water for 30 min. The final concentration of the siRNA was adjusted to 1 μg/mL using water (pH 7.3). The diameters of the complexes were determined using a Zetasizer (Malvern Instruments, Malvern, UK) with the He/Ne laser at a detection angle of 173° and a temperature of 25 °C.

4.4. Electrophoresis of the polymer/siRNA complex

For the electrophoresis experiment, various concentrations of the polymer were mixed with the siRNA in ultrapure distilled water (Invitrogen) at room temperature for 30 min, and then analyzed by 19% polyacrylamide gel electrophoresis.

4.5. Delivery of polymer/siRNA complexes into mice by direct injection

All animal studies were performed in accordance with the Guidelines for Animal Experiments, established by the Ministry of Health, Labour and Welfare of Japan, and by the National Cardiovascular Center Research Institute. Male 6-week-old BALB/c mice (CLEA Japan Inc., Osaka, Japan) weighing approximately 22 g were used in this study. The mice were maintained in a temperature-controlled room (22 °C) with a 12-h light-dark cycle and were provided with a standard pellet diet (CE-2; CLEA Japan) and water ad libitum. One week after arrival, mice were divided into two groups, the hydrodynamics injection group and the non-hydrodynamics injection group. In the hydrodynamics injection group, 2 mL of 5% glucose solution containing each polymer/siRNA complex was injected, whereas in the non-hydrodynamics injection group, 0.2 mL was injected. For the hydrodynamics-based procedure, solutions were injected over 6–8 s into the tail vein using a 27-gauge needle. The mice were sacrificed 1 or 3 h after the injections, and thereafter each tissue type (lung, heart, liver, spleen, and kidney) was excised. Images were obtained with the Maestro In Vivo Imaging System (Cambridge Research & Instrumentation, Woburn, MA, USA).

Acknowledgment

This work was supported by a research grant from the Ministry of Health, Labour and Welfare (MHLW) and by the Program for Promotion of Fundamental Studies in Health Sciences of the National Institute of Biomedical Innovation (NIBIO), Japan.

Supplementary data

Supplementary data (Tables S1 and S2 describing molecular parameters of polymer and zeta potential of PEI-pullulan/siRNA complex, respectively) associated with this article can be found, in the online version, at doi:10.1016/j.bmc.2010.04.031.

References and notes

1. Kim, D. H.; Rossi, J. J. *Biotechniques* **2008**, *44*, 613.
2. Zhang, N.; Tan, C.; Cai, P.; Zhang, P.; Zhao, Y.; Jiang, Y. *Bioorg. Med. Chem.* **2009**, *17*, 2441.
3. Fattal, E.; Bochot, A. *Int. J. Pharm.* **2008**, *364*, 237.
4. Ueno, Y.; Kawada, K.; Naito, T.; Shibata, A.; Yoshikawa, K.; Kim, H.-S.; Wataya, Y.; Kitade, Y. J. *Bioorg. Med. Chem.* **2008**, *16*, 7698.
5. Perez, A. P.; Romero, E. L.; Morilla, M. J. *Int. J. Pharm.* **2009**, *380*, 189.
6. Uduehi, A. N.; Stammberger, S.; Frese, S.; Schmid, R. A. *Eur. J. Cardiothorac. Surg.* **2001**, *20*, 159.
7. Wightman, L.; Kircheis, R.; Rossler, V.; Carotta, S.; Ruzicka, R.; Kursa, M.; Wagner, E. *J. Gene Med.* **2001**, *3*, 362.
8. Kawakami, S.; Ito, Y.; Charoensit, P.; Yamashita, F.; Hashida, M. *J. Pharmacol. Exp. Ther.* **2006**, *217*, 1382.
9. Jeong, G. J.; Byun, H. M.; Kim, J. M.; Yoon, H.; Choi, H. G.; Kim, W. K.; Kim, S. J.; Oh, Y. K. *J. Controlled Release* **2007**, *118*, 118.
10. Aravindan, L.; Bicknell, K. A.; Brooks, G.; Khutoryanskiy, V. V.; Williams, A. C. *Int. J. Pharm.* **2009**, *378*, 201.
11. Yamaoka, T.; Tabata, Y.; Ikada, Y. *Drug Deliv.* **1993**, *1*, 75.
12. Kaneo, Y.; Tanaka, T.; Nakano, T.; Yamaguchi, Y. *J. Controlled Release* **2001**, *70*, 65.
13. Mehvar, R. *Curr. Pharm. Biotechnol.* **2003**, *4*, 283.
14. Goula, D.; Benoist, C.; Mantero, S.; Merlo, G.; Levi, G.; Demeneix, B. A. *Gene Ther.* **1998**, *5*, 1291.
15. Ogris, M.; Brunner, S.; Schuller, S.; Kircheis, R.; Wagner, E. *Gene Ther.* **1999**, *6*, 595.
16. Liu, F.; Song, Y. K.; Liu, D. *Gene Ther.* **1999**, *6*, 1258.
17. Kobayashi, N.; Hirata, K.; Chen, S.; Kawase, A.; Nishikawa, M.; Takakura, Y. *J. Gene Med.* **2004**, *6*, 455.
18. Fahrmeir, J.; Gunther, M.; Tietze, N.; Wagner, E.; Ogris, M. *J. Controlled Release* **2007**, *122*, 236.
19. Kircheis, R.; Schuller, S.; Brunner, S.; Ogris, M.; Heider, K. H.; Zauner, W.; Wagner, E. *J. Gene Med.* **1999**, *1*, 111.
20. Chollet, P.; Favrot, M. C.; Hurbin, A.; Coll, J. L. *J. Gene Med.* **2002**, *4*, 84.
21. Goula, D.; Becher, N.; Lemkine, G. F.; Normandie, P.; Rodrigues, J.; Mantero, S.; Levi, G.; Demeneix, B. A. *Gene Ther.* **2000**, *7*, 499.
22. Boletta, A.; Benigni, A.; Lutz, J.; Remuzzi, G.; Soria, M. R.; Monaco, L. *Hum. Gene Ther.* **1997**, *8*, 1243.
23. Moghimi, S. M.; Symonds, P.; Murray, J. C.; Hunter, A. C.; Debska, G.; Szewczyk, A. *Mol. Ther.* **2005**, *11*, 990.

Ann Nucl Med (2010) 24:1–11
DOI 10.1007/s12149-009-0323-8

ORIGINAL ARTICLE

Development of motion correction technique for cardiac ^{15}O-water PET study using an optical motion tracking system

Kazuhiro Koshino · Hiroshi Watabe · Shinji Hasegawa · Takuya Hayashi · Jun Hatazawa · Hidehiro Iida

Received: 19 August 2009 / Accepted: 9 October 2009 / Published online: 3 December 2009

Abstract
Objective Cardiac ^{15}O-water PET studies provide an accurate quantitation of regional myocardial blood flow (rMBF). We developed a motion correction system using an optical motion-tracking device to detect a subject's global movement for cardiac study.
Methods PET studies were carried out on a cardiac phantom and a healthy volunteer at rest. The three-dimensional locations of the markers attached to the subjects during scans were measured using an optical motion-tracking system. In the phantom study, we performed a transmission scan and seven ^{18}F emission scans of a baseline and with artificial misalignment of shifts and rotations. The correlation coefficients between the baseline and the other images before and after the corrections for the misalignment were calculated. In the human study, we performed a ^{15}O-water dynamic scan with a transmission and axially 30 mm-shifted transmission scans. Motion of the subject was estimated by the information from the system, and was corrected on each sinogram using attenuation maps realigned to dynamic frames. Reconstructed dynamic images were then realigned to the transmission data. We calculated rMBF values for nine segments and myocardial images from the emission images, which were reconstructed with the first attenuation map (reference) and with the misaligned attenuation map before and after our corrections.
Results In the phantom study, the correlation coefficients were improved from 0.929 ± 0.022 to 0.987 ± 0.010 (mean $\pm$ SD) after the corrections. In the human study, the global and cyclic movements were detected. The cyclic movement due to respiration was smoothed by frame-averaging, and reasonable information of the global movement was obtained. The rMBF value (mean $\pm$ SD) was 0.94 ± 0.12 mL/min/g for the reference. The rMBF values using the misaligned attenuation map changed from 1.03 ± 0.21 to 0.93 ± 0.11 mL/min/g after the correction, and spurious defects in myocardial images were also recovered.
Conclusions Our technique provided reasonable information for correcting the global movement of the subject. It was shown that this system was applicable to detect and correct subject movement in cardiac PET studies at rest.

Keywords Myocardial blood flow · PET · Motion correction · Attenuation correction · ^{15}O-labeled water

K. Koshino (✉) · H. Watabe · H. Iida
Department of Investigative Radiology,
National Cardiovascular Center Research Institute,
5-7-1 Fujishirodai, Suita, Osaka 565-8565, Japan
e-mail: koshino@ri.ncvc.go.jp

S. Hasegawa
Department of Cardiology, Osaka Koseinenkin Hospital,
Osaka, Japan

T. Hayashi
Functional Probe Research Laboratory,
RIKEN Center for Molecular Imaging Science, Hyogo, Japan

J. Hatazawa
Department of Nuclear Medicine and Tracer Kinetics,
Osaka University Graduate School of Medicine, Osaka, Japan

Introduction

Motion of a patient during a positron emission tomography (PET) scan can cause deterioration in image quality and quantitative accuracy. Several techniques have been

proposed for motion compensation in neuroimaging [1–7]. In cardiac PET studies, effects of wall contractile and respiratory motion can be smoothed in the temporary sampled PET images, but global movement of the patients during the relatively long scanning period is still a significant source of errors [8–11].

It was shown that misalignment by a 20-mm shift in the lateral/septal direction between transmission and ^{18}F-fluorodeoxyglucose (^{18}FDG) emission scans caused a 30% change in regional activity in cardiac ^{18}F-FDG PET [8]. To align two ^{18}F-FDG emission images acquired on different days, Bacharach et al. [11] proposed a registration technique based on the rigid body model using the transmission images by assuming no misregistration between transmission and emission data sets.

Cardiac ^{15}O-water PET studies provide quantitative information with regard to the viabilities of myocardium using the myocardial blood flow (MBF), coronary flow reserve, and perfusable tissue index [12–19]. Naum et al. [20] demonstrated that the movement occurred during dynamic scans with cycling. They proposed a method to correct for the motion during a single dynamic scan, and among different sessions, by aligning the dynamic frames of ^{15}O-water images using two external radioactive markers placed on the back of a subject. Although their technique did not provide correction for misalignment between transmission and emission data, reasonable improvement in calculated MBF values was demonstrated.

Correcting the misalignment between the transmission and emission data is a challenging task because the image contrast of transmission images differs from that of emission images. The distribution of ^{15}O-water also varies dramatically in regions of the right and left ventricles, myocardium, and other organs over time. Additionally, the image quality of PET with ^{15}O-water is worse than that with other radioligands due to the short half life of ^{15}O, which makes image registration difficult.

In this paper, we describe a novel approach using an optical motion-tracking system for detecting the subject's global movement during the relatively long study period, as an extension of the early studies of Watabe et al. [4]. The proposed technique provided correction for misalignment between dynamic emission sinograms, and also provided accurate attenuation correction, in which misalignment between attenuation map and each emission sinogram was corrected in the reconstruction stage.

First, the inherent accuracy of our system was evaluated. Then, the system was validated on a cardiac phantom study for artificial misalignment between an attenuation map and emission data. Correction for global movement obtained by monitoring the locations of external markers on chest skin was validated in a ^{15}O-water cardiac PET study in a healthy volunteer at rest.

Materials and methods

Hardware-based position monitoring system

To detect motion of a subject, we adopted an optical motion-tracking device in which targets attached to the chest skin are monitored. The motion compensation approach using an optical motion-tracking system has been previously validated in brain PET studies [3–7]. We applied this approach to the cardiac PET studies. Figure 1a shows an optical motion-tracking system, POLARIS (Northern Digital Inc., Canada). The POLARIS has two charge-coupled-device cameras, and provides the 3D position of a target. The three-dimensional position is measured in the form of 6 degrees of freedom: three rotational angles, and three translational directions. The manufacturer reports that the accuracy of the rotational angle and translation are better than 0.3° and 0.5 mm, respectively. Figure 1b shows a target with four infrared-reflective markers and supporting post. The target and supporting post made of carbon resin were pinned with two fluoroplastic screws. Figure 1c shows the position calibration tool used to convert the locations of subject positions in the POLARIS coordinate into PET coordinates. Figure 1d represents the schematic diagram of our system. Locations of targets attached to the chest skin of the subject and the gantry of a PET scanner were measured with the POLARIS. The target on the gantry of the PET scanner was used as a reference in order to convert the subject's positions from the POLARIS coordinate to the PET coordinate. Figure 1e shows an example of the experimental setup with a healthy volunteer in the cardiac PET study. Two targets were attached to the chest skin of the subject. Three legs of the supporting post were attached to the skin of the subject using surgical tape. The axial field-of-view (FOV) of the PET scanner used in the human study, HEADTOME-V tomography (SHIMADZU Corp., Kyoto, Japan), was 200 mm, and the gantry diameter was 850 mm [21]. The geometries of targets attached to the thoracic surface were 85×85 mm^2 (the left-hand target in Fig. 1e, target 1) and 65×90 mm^2 (the right-hand target in the Fig. 1e). The heights of supporting posts for target 1 and target 2 were 50 and 42 mm, respectively. We calculated the subject's positions in the PET coordinate by measuring the locations of the target with four infrared-reflective markers (the primary target). Another target was used as a reserve in cases when the primary target was hidden from the FOV of the POLARIS.

Motion correction

The rigid motion correction technique employed is an extension of the previous work for brain PET studies by

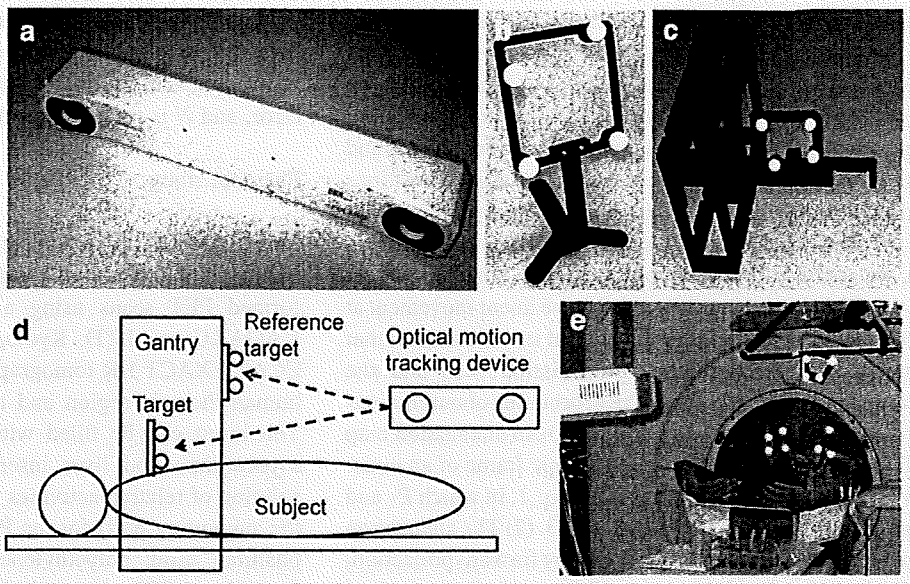

Fig. 1 Our motion correction system. **a** Optical motion-tracking device. **b** Target consists of infrared-reflective markers with supporting post. **c** Position calibration tool with a target. **d** Schematic diagram of the system. Locations of the targets on the subject and the gantry were measured with the optical motion-tracking device. **e** An example of the experimental configuration

Watabe et al. [4]. We consider four coordinates: the POLARIS C_S, a target on a PET gantry for reference C_G, a target attached on a subject C_T, and the PET scanner C_P. By measuring the location and orientation of each target attached to the subject and the gantry using the POLARIS, we obtained a 4 × 4 transformation matrixes, $T_{T\to S}$ from C_T to C_S, and $T_{G\to S}$ from C_G to C_S, respectively. Motion matrix $M_{P_1\to P_2}$ from a position $P_1 = P(t_1)$ to another position $P_2 = P(t_2)$ in the PET coordinate is written as follows [4]:

$$M_{P_1\to P_2} = T_{G\to P}T_{G\to S}^{-1}T_{T_1\to S}T_{T_2\to S}^{-1}T_{G\to S}T_{G\to P}^{-1} \quad (1)$$

where T_1 and T_2 are positions in target coordinates corresponding to positions P_1 and P_2 in the PET coordinate. $T_{G\to P}$ is the matrix to transform a position from the gantry coordinate to the PET coordinate. The matrix is given by the following equation:

$$T_{G\to P} = T_{S\to P}T_{G\to S} \quad (2)$$

$T_{S\to P}$ is the matrix which relates the POLARIS and PET coordinates and is obtained by position calibration.

The point source was embedded in a given position of a target, which is fixed on the calibration tool shown in Fig. 1c. By measuring the position of the point source using the POLARIS, the position $P_S = (x_S, y_S, z_S)$ of the point source in the POLARIS coordinate is calculated using the known position $P_T = (x_T, y_T, z_T)$ in the target coordinate and $T_{T\to S}$, as $P_S = T_{T\to S}P_T$. The position $P_P = (x_P, y_P, z_P)$ in the PET coordinate is also obtained from the reconstructed emission image. By changing the position of the target, in which the point source is embedded, $T_{S\to P}$ is calculated using the least-squared-fit between the pairs of P_Ss and P_Ps. The PET coordinate was

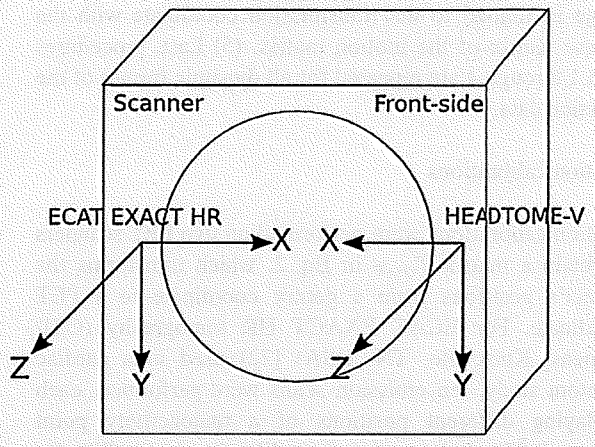

Fig. 2 PET coordinates defined by position calibrations

defined by the position calibration as shown in Fig. 2. The positions of subjects in the PET coordinate will be discussed in the following.

To correct a subject's movements during a dynamic acquisition of an emission scan with multiple frames, we estimated the heart locations from the locations of the target, which are measured by the POLARIS. The displacement of the COG of the heart's position from during the transmission scan to during each dynamic frame of the emission scan is given by

$$\begin{aligned} H^F - H^{TCT} &= \frac{1}{L}\sum_t^F H(t) - \frac{1}{N}\sum_t^{TCT} H(t) \\ &= \frac{1}{L}\sum_t^F [P(t) + \Delta(t)] - \frac{1}{N}\sum_t^{TCT} [P(t) + \Delta(t)] \end{aligned} \quad (3)$$

where H^{TCT} and H^{F} are the averaged COGs of the heart positions during the transmission and the dynamic frame, $H(t)$ and $P(t)$ are the COGs of positions of the heart and the target at time t, $\Delta(t)$ is a term representing a non-rigid relation for positions at time t between the heart and the target, L and N are the numbers of measurements of the target's positions by the POLARIS during acquisition of the dynamic frame and the transmission scan, respectively. For motion correction, we assumed the rigid body model, in which the target and the COG of the heart's position have linear movement at least in the FOV of a PET scanner, that is, we assumed that summations of $\Delta(t)$ for the transmission scan and the dynamic frame equal to zero. The procedures of our motion-correction technique are as follows: (1) An attenuation map is aligned to the coordinate of a dynamic frame of an emission scan using the motion matrix in Eq. 1, in which P_1 and P_2 are $\Sigma^{TCT}P(t)/N$ and $\Sigma^{F}P(t)/L$ in Eq. 3. (2) The attenuation map is then converted to its sinogram by forward projection. (3) Each sinogram of the dynamic frames is reconstructed with the realigned attenuation sinogram. (4) The emission image is aligned to the transmission coordinate with the inverse matrix of the motion matrix. (5) Last, procedures from 1 through 4 are repeated for all dynamic frames of the emission data.

Position calibrations

Position calibrations were performed on two PET scanners to obtain a matrix $T_{G\to P}$ in Eq. 2, which transforms the subject's positions from a gantry coordinate to a PET coordinate. For ECAT EXACT HR tomography (CTI/Siemens, Knoxville, TN, USA) [22] used in a cardiac phantom study, ten emission scans were performed, each displaying different positions of a radioactivity point source of ^{18}F solution, using the calibration tool in Fig. 1b. For the PET scanner used in a healthy volunteer study, 14 emission scans were performed with the ^{18}F solution point source and calibration tool.

The accuracy of the calibrations was evaluated from $T_{G\to S}$ and $T_{S\to P}$ in Eq. 2. The accuracy of $T_{G\to S}$ part was evaluated by determining the standard deviation (SD) of rotational angles and translations calculated from position data of the gantry, because $T_{G\to S}$ depends on only the accuracy of the measurements in regard to the POLARIS. To evaluate the accuracy of $T_{S\to P}$ part, we calculated errors between a position of a point source P_P, and the approximation position using $T_{S\to P}$, $P_X = T_{S\to P}P_S$:

$$e(i,k) = P_X(i,k) - P_P(i,k) \tag{4}$$

$$\mathrm{RMSE}(i) = \sqrt{\sum_{k=x,y,z} |P_X(i,k) - P_P(i,k)|^2} \quad (k = X, Y, Z \text{ and } i = 1, \ldots, N) \tag{5}$$

where $e(i, k)$ is the approximation error of a point source in the ith position for each direction, X, Y, and Z are orthogonal axes in Fig. 2, RMSE(i) is the root mean square error, and N is the number of positions of a point source.

Phantom study

To validate our correction technique for the misregistration between the attenuation map and emission data, we performed PET scans using a cardiac phantom (KYOTO KAGAKU co., LTD, Kyoto, Japan, type HL-D) and the ECAT EXACT HR tomography. The phantom mimics the human thoracic region and has cardiac and liver inserts. The insert can be filled with radioisotope solution. The myocardium and liver inserts were filled with the ^{18}F solution of relative activities of 1 and 4. A target (without the supporting port) for the POLARIS was attached to the phantom using polyethylene cross tape. Then, we performed a 1,000-s transmission scan for attenuation corrections. After the transmission scan, seven ^{18}F emission scans were performed with a set of single frame data for 180 s. The first scan was the baseline (scan #1), in which there was no misalignment to the transmission. For the following three emission scans (scan #2–4), the phantom was moved in the X, Y, and Z directions. For the other three scans, the phantom was rotated about the X, Y, and Z axes (scan #5–7). The phantom's positions were measured with the POLARIS.

The reconstructed images before and after the correction were obtained using an FBP (filtered back-projection) algorithm with a Gaussian filter of 6 mm FWHM (full-width at half-maximum). The matrix size and voxel size of images were 128 × 128 × 47 and 4.4 × 4.4 × 3.1 mm^3, respectively. All emission data were corrected for physical decay of ^{18}F with base time as the start of the first emission scan, and all of the emission images were reoriented to the short axis using a transformation matrix.

To evaluate the effects of the corrections, we calculated correlation coefficients for myocardial regions between the baseline and misaligned emission images, both before and after the corrections.

Human study

A cardiac ^{15}O-water PET study was performed on a healthy volunteer (male, 32 years old) using the HEADTOME-V tomography in order to validate use of the external markers on the chest skin and also to evaluate the effects of the global movement on the quantification of MBF by artificial misalignment between attenuation and emission data. The healthy volunteer gave written informed consent according to a protocol approved by the Ethical Committee and

Internal Review Board of Osaka University. The PET study consisted of a 20-min transmission scan, an 8-min ^{15}O-CO emission scan for blood pool imaging, a 6-min ^{15}O-water emission scan with 26 dynamic frames (12 × 5, 8 × 15 and 6 × 30 s), and a second 20-min transmission scan. All scans were acquired in a 2D acquisition mode. The radioactivity of inhaled ^{15}O-CO gas was 3.2 GBq. ^{15}O-water was injected via the left brachial vein; activity was 1.1 GBq for 40 s. All scans were performed without pharmacological stress. To investigate the accuracy of the POLARIS for tracking the locations of the target attached to the thorax skin of the subject, the couch of the PET scanner was moved +30 mm along the axial direction before the second transmission scan, corresponding to the Z direction in Fig. 2, with the subject lying on the couch. It was expected that the shift in the $+Z$ direction caused the artificial deterioration of image quality and quantitative accuracy in especially the anterior and lateral regions. The subject's positions during the scans were monitored by the POLARIS, at a frequency of one sample per second.

The reconstructed images for the four cases were obtained using an FBP algorithm with a Gaussian filter of 9 mm FWHM. The matrix and voxel sizes of the reconstructed images were 128 × 128 × 63 and 2.03 × 2.03 × 3.13 mm^3. No scatter correction was performed during the image reconstruction stage.

Regional MBF values were estimated for four cases. Case 1: the first attenuation map and emission data, case 2: the first attenuation map and emission data with correction for the subject's motions, case 3: the second attenuation map and the emission data, case 4: the second attenuation map and the emission data after the correction for the subject's motions and the 30-mm-shifted misalignment. Differences in the MBF values for cases 1 and 2 were considered to indicate effects from the correction for the frame-averaged motion if the subject's motion was small. Differences in MBF values for cases 1 and 3 could indicate errors in the quantification of MBF caused by the artificial misalignment between the second attenuation map and the emission data. The lack of any difference in MBF values for cases 1 and 4 indicated that our technique tracked the shift of the target on the thorax skin accurately and corrected the misalignment. In order to generate cases 2 and 4, the positions P_1 and $P_2^{(j)}$ in Eq. 1 were calculated as averaged COGs of the subject's positions during the first and second transmission scans and the jth dynamic frame of ^{15}O-water or C^{15}O emission scan. Using Eq. 1 with P_1 and $\{P_2^{(j)}\}$, we performed frame-by-frame motion corrections for all dynamic frames of emission data. Due to the fact that the PET scanner did not provide a dynamic transmission scan, we assumed that the subject did not move during the transmission scan.

For quantification of MBF, we employed a compartment analysis model proposed by Iida et al. [13], which provided corrections for spillover from a left ventricle and partial volume effect and generated a MBF value in units of mL/min/g of perfusable tissue. All transmission and emission images were reoriented to the short axis. To calculate tissue time activity curves, regions of interest (ROIs) were drawn in nine myocardial regions: apical, mid-anterior, mid-lateral, mid-posterior, mid-septal, basal-anterior, basal-lateral, basal-posterior, and basal-septal regions. To avoid spillover effects from the right ventricle, the sizes of ROIs in septal regions were smaller than those in other regions. Another ROI was drawn on the left ventricle in order to estimate the arterial input function [19]. These ROIs were manually and independently drawn for the four cases. In addition, to validate the consistency between the quantitative results of MBF values and the quality of the images, we calculated the build-up and washout phase images [23] for the four cases. The build-up and washout phase images were obtained by subtracting a blood pool image from summed images of early (0–180 s) and later (180–360 s) frames of a ^{15}O-water image.

We evaluated the magnitude of the subject's motions in the PET coordinate during each scan. We defined position P_1 in Eq. 1 as the position at the start of the first transmission scan, and position P_2 as the position at an arbitrary time during a transmission or an emission scans. The rotational angles and translations for arbitrary times were obtained using Eq. 1. We represented motion during a scan in the form of mean ± SD for each rotational angle and translation.

Results

Position calibrations

Table 1 shows the inherent accuracy of our system in the two PET scanners. Values of SDs for rotations and translations obtained from $T_{G\to S}$ data were very small. Table 1 also shows the approximation errors (mean ± SD) occurred while transforming the positions of a point source from the POLARIS coordinate to the PET coordinate using $T_{S\to P}$. There was no bias in any direction in either scanner. Each value of RMSE was smaller than the spatial resolution of the corresponding scanner [21, 22].

Cardiac phantom study

Table 2 lists the observed misalignment from the reference position of the phantom in the transmission scan and the correlation coefficients between the reference image and the misaligned images before and after the corrections (mean ± SD; 0.929 ± 0.022 and 0.987 ± 0.010). The

Table 1 Inherent accuracy of the motion correction system in the two PET scanners

Scanner	$T_{G\to S}$						$T_{S\to P}$				# of point positions
	Rotational angle (deg)			Translation (mm)			e_x	e_y	e_z	RMSE	
	r_x	r_y	r_z	t_x	t_y	t_z					
ECAT EXACT HR	0.0	0.0	0.0	0.0	0.0	0.0	0.0 ± 0.8	0.0 ± 0.9	0.0 ± 0.8	1.3 ± 0.4	10
HEADTOME-V	0.0	0.0	0.0	0.0	0.0	0.1	0.0 ± 1.5	0.0 ± 1.6	0.0 ± 0.6	2.3 ± 0.2	14

Standard deviations of rotational angles and translations obtained from $T_{G\to S}$ data and approximation errors (mean ± SD in mm) by transforming positions of a point source from the POLARIS coordinate to the PET coordinate using $T_{S\to P}$. Columns $T_{G\to S}$, r_x, r_y and r_z denote SDs of rotational angles about three orthogonal *X*, *Y*, and *Z* axes, respectively. t_x, t_y and t_z denote SDs of translations along three orthogonal axes, respectively. Columns $T_{S\to P}$, e_x, e_y, and e_z denote average values (mean ± SD in mm) of $e(i, X)$, $e(i, Y)$, and $e(i, Z)$, respectively. $e(i, k)$ was defined in Eq. 4. *RMSE* denotes an average value (mean ± SD in mm) of *RMSE*(*i*), defined in Eq. 5

Table 2 The observed misalignment and correlation coefficients for the phantom study

Scan no.	Rotation (deg)			Translation (mm)			Correlation coefficient	
	r_x	r_y	r_z	t_x	t_y	t_z	Before MC	After MC
2	0.0	0.2	5.1	35.7	0.8	−3.4	0.896	0.997
3	0.0	−1.0	1.3	0.9	35.2	3.2	0.938	0.995
4	0.0	−0.2	0.9	5.9	0.1	42.8	0.917	0.971
5	13.1	1.4	0.4	1.9	22.5	17.1	0.926	0.986
6	2.4	−15.6	−2.1	10.9	3.8	4.7	0.938	0.982
7	−0.6	1.8	−13.5	13.4	11.9	−9.5	0.960	0.992

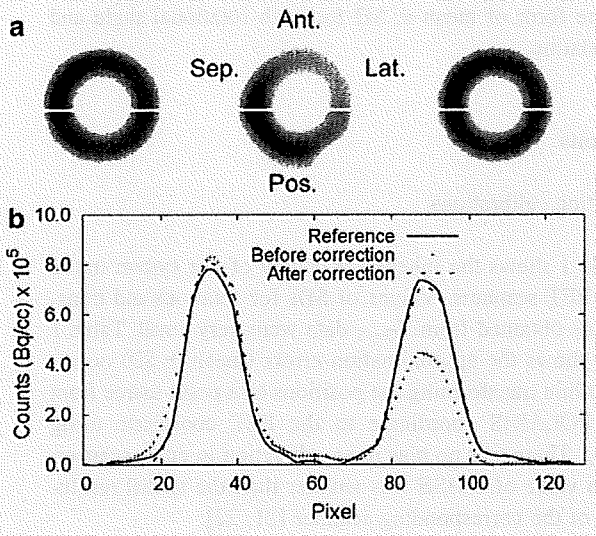

Fig. 3 Reconstructed and reoriented images of the phantom. **a** Reconstructed images. *Left*, *mid*, and *right* columns represent the reference emission image (no misalignment), the second emission images before correction for misalignment, and the second emission images after correction for the misalignment, respectively. **b** Profiles at the level of white lines in images. *Solid line*, *cross symbols*, and *dashed lines* represent the first emission image, the second emission images before correction, and the second emission images after correction, respectively

effects of our correction technique are demonstrated in Fig. 3. The left column in Fig. 3a is the reference emission image (no misalignment). The middle and right columns represent the emission images with the misalignment of the *X*-direction before and after the corrections. For the image in the middle column, only the position was transformed to the transmission coordinate after the reconstruction. Figure 3b represents line profiles at the level of white lines in the slices.

Human study

Table 3 summarizes the observed movements of the subject during scans relative to the beginning of the first transmission scan, in the form of rotational angles about and translations along three orthogonal axes. It was observed that the magnitude of the average parts of the rotational angles and translations tended to increase. The value of t_z changed from -1.8 ± 0.6 to 28.3 ± 0.6 mm between the ^{15}O-water emission and the second transmission scan mainly because of the 30-mm shift of the couch as well as the motions of the subject. There was little change in the SD in any rotational angle or translation among the scans.

Figure 4 shows motion parameters during ^{15}O-water scan. Figure 4a and b represent the sample-by-sample and frame-averaged translations. Figure 4c and d shows the sample-by-sample and frame-averaged rotational angles.

Table 4 shows that the MBF values (mean ± SD), which were obtained from nine myocardial segments, were 0.94 ± 0.12, 0.91 ± 0.13, 1.03 ± 0.21, and 0.93 ± 0.11 mL/min/g for the four cases. The values for cases 1 and 2 were obtained from the emission data and the first attenuation map before and after motion correction. The values for cases 3 and 4 were obtained from the emission data and the second attenuation map before and after the corrections for the subject's motions and the 30-mm shift of the couch. There were significant

Table 3 Observed movements (mean ± SD) of the healthy volunteer during scans relative to the beginning of the first transmission scan

Scan	Rotational angle (deg)			Translation (mm)		
	r_x	r_y	r_z	t_x	t_y	t_z
TCT 1	−0.1 ± 0.2	−0.4 ± 0.2	−0.2 ± 0.2	0.7 ± 0.5	1.3 ± 0.6	1.0 ± 0.8
$C^{15}O$	0.0 ± 0.2	−0.1 ± 0.2	−0.7 ± 0.1	2.6 ± 0.3	1.0 ± 0.5	−1.7 ± 0.7
^{15}O-water	0.4 ± 0.2	0.0 ± 0.1	−0.7 ± 0.1	2.7 ± 0.2	1.3 ± 0.4	−1.8 ± 0.6
TCT 2	−0.4 ± 0.2	0.7 ± 0.2	−2.0 ± 0.1	3.7 ± 0.3	2.6 ± 0.5	28.3 ± 0.6

r_x, r_y, and r_z denote rotational angles (degrees) about X, Y, and Z-axes, respectively. t_x, t_y, and t_z denote translations (mm) along *X*, *Y*, and *Z* axes, respectively

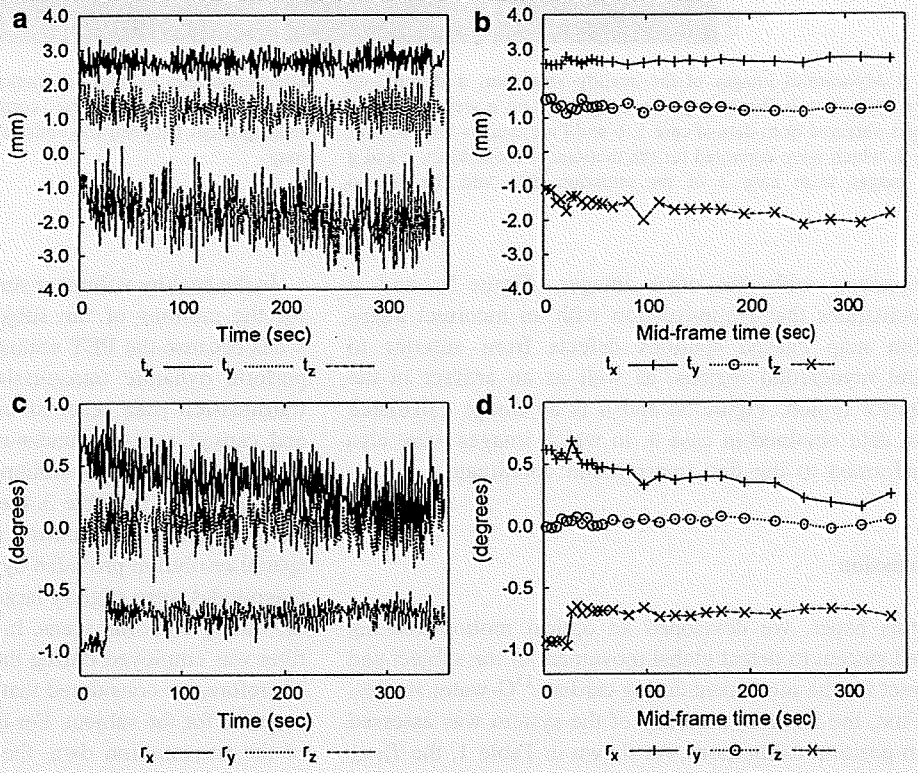

Fig. 4 Motion parameters during ^{15}O-water study on the healthy volunteer. **a**, **b** Sample-by-sample and frame-averaged translations. **c**, **d** Sample-by-sample and frame-averaged rotational angles

Table 4 MBF values (mL/min/g of perfusable tissue) of the healthy volunteer

Myocardial region	Case			
	1	2	3	4
Apical	1.05	1.00	0.99	1.05
Mid-anterior	0.92	0.89	1.26	0.99
Mid-lateral	0.93	0.89	1.38	0.89
Mid-posterior	1.14	1.16	0.96	1.01
Mid-septal	1.05	1.06	1.08	1.12
Basal-anterior	0.87	0.80	1.18	0.80
Basal-lateral	0.86	0.82	0.95	0.84
Basal-posterior	0.88	0.83	0.84	0.86
Basal-septal	0.73	0.72	0.65	0.82
Mean ± SD	0.94 ± 0.12	0.91 ± 0.13	1.03 ± 0.21	0.93 ± 0.11

differences in the mid-anterior and mid-lateral regions as well as the basal-anterior regions between cases 1 and 3.

Figure 5 demonstrates the influence of misalignment between an attenuation map and emission data on the quality of myocardial images, as well as the effect of our correction technique. Figure 5a–f represent the build-up and washout phase images of middle myocardial obtained from the ^{15}O-water data. Anterior, lateral, posterior, and septal regions of myocardia were arranged in a clockwise manner. Figure 5a and e was obtained from the data of case 1, and Fig. 5b and f was calculated from the data obtained in case 2. Figure 5c and g was derived from the data in case 3, and only positions of reconstructed images were transformed to the first transmission coordinate after reconstructions for visual

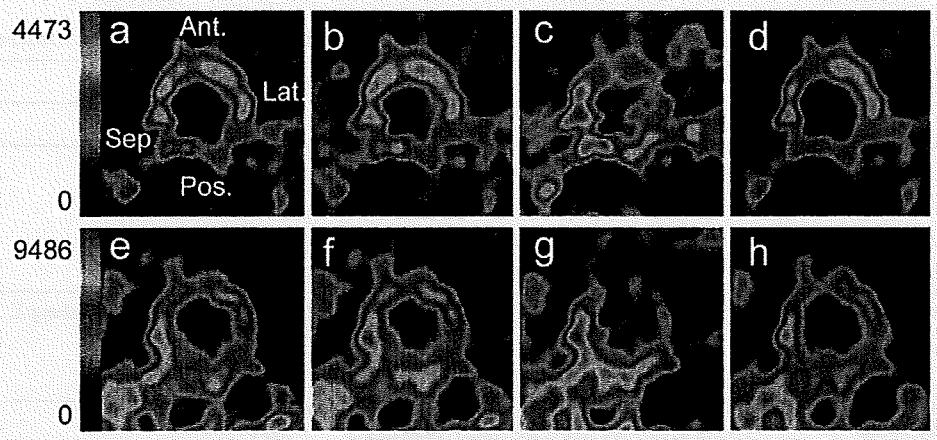

Fig. 5 Myocardial images of the healthy volunteer. **a–d** Build-up phase images. **e–h** Washout phase images. **a** and **e** were reference images obtained from data of case 1. **b** and **f** are images from data of case 2, which were corrected for the motions of the subject. **c** and **g** are images from case 3 of the emission data and the second attenuation map without our motion corrections. **d** and **h** are images from case 4, which were corrected for the motions and the misalignment between the emission data and the second attenuation map

comparison with the other images. Figure 5c and g demonstrates that reconstruction with an incorrect attenuation map caused spurious defects from anterior to lateral myocardial regions, as well as an artifact in the posterior region. Figure 5d and h is an image calculated from data obtained in case 4, in which images were also transformed to the first transmission coordinate.

Discussion

In this paper, we developed an optical motion-tracking based system to detect global movement of the subject and correct for the movement during cardiac ^{15}O-water studies.

First, the inherent accuracy of the system was assessed from position calibrations. As shown in Table 1, the $T_{G\rightarrow S}$ part could be negligibly small compared with the magnitude of the subject's motions in Table 3 and Fig. 4. For the $T_{S\rightarrow P}$ part shown in Table 1, there was no bias in any direction. The value of RMSE for each scanner was smaller than the spatial resolution of the scanner [21, 22]. Therefore, it was considered that the position calibrations provided a sufficient level of accuracy for our motion corrections.

To validate the present technique, we performed a cardiac phantom study. As shown in Fig. 3a, a defect and blurred region from the anterior to the lateral, which was mainly caused by a 5.1° rotation about the Z axis and a 35.7 mm shift along the X axis, was recovered using the present technique. The effect of the present technique was also shown more objectively by the correlation coefficients and profile comparison in Fig. 3b.

In the healthy volunteer study, no correction was applied for the motions of the subjects during the transmission scans because the PET scanners do not have the ability to perform dynamic transmission scans. Motions during a transmission scan resulted in a blurred attenuation map, and caused over- or under-estimation of the radioactive concentration in myocardium of ^{15}O-water images. However, as shown in Table 3, the magnitudes of the mean and SD during the transmission scans were smaller than the spatial resolution provided by the PET scanner, even if the magnitudes were slightly larger than those of the mean and SD during emission scans. In addition, a 9-mm smoothing filter was employed during the image reconstruction stage. Therefore, we considered that valid transmission data were acquired for the subject. For the same reason as in the case of the transmission data, the emission data of ^{15}O-water scan were acquired properly. So we used the data of case 1 as the reference for the other cases.

The global movement and cyclic movement of the target were observed as shown in Fig. 4a and c. The cyclic movement was attributed to respiration. From Fig. 4b and d, the cyclic movement was smoothed by frame-averaging. In addition, the regional MBF values (Table 4) and the myocardial images (Fig. 5) of cases 1 and 2, which were derived from the same transmission and emission scans before and after the motion correction, were nearly the same. This result indicated that our system provided reasonably accurate information about the global movement.

In case 3, in which no correction for the subject's motions and the 30-mm shift between the emission data and the second attenuation map was applied, the MBF values for the mid-anterior, mid-lateral, and basal-anterior regions were

significantly larger than the reference values. This overestimation was associated with spurious defects from the anterior to lateral regions, as shown in Fig. 5c and g. In case 4 with our correction technique, the MBF values for myocardial regions, in which overestimated MBFs were obtained for the corresponding regions in case 3, were similar to the reference values. The image quality in Fig. 5d and h was also nearly the same as in Fig. 5a and e. Figure 5d shows a clearly delineated contour of the myocardial region similar to the contour in Fig. 5a. The spurious defects from the anterior to lateral regions in Fig. 5g were recovered in Fig 5h. Owing to these results, the present technique tracked the location of the external target attached to the chest skin accurately, and then corrected the artificial misalignment during transmission and emission scans. Figure 5 not only shows the effects of our correction technique, but also suggests that the use of an attenuation map with large global movement could cause the appearance of spurious defects in myocardial imaging with ^{15}O-water PET.

Several listmode-based motion correction techniques have hitherto been proposed [1, 3–7]. Compared to these techniques, our technique provides poorer time resolution, even though our technique was applied to an emission scan consisting of dynamic frames with shorter duration. Listmode-based methods, however, require wide band transmission and high computational power for manipulating the listmode event data, especially under high count rates. For the listmode-based methods, in which data processing is conducted prior to the motion correction, corrections for detector efficiency, detector geometry, and crystal interferences are important issues, especially in the case of scanners with gaps between detectors or no intersection of motion-corrected LOR with detector(s). For our technique with 2D acquisition mode, the sinogram data are simply normalized by the built-in software of the used PET scanners. Our technique could shorten the processing time by re-binning the listmode data during the period when substantial movement is detected, and then correcting the re-framed dynamic sinogram. Furthermore, our technique is applicable to many commercially available PET scanners, which often have no feasibility of listmode acquisition.

Instead fixating the POLARIS on a certain position, such as the gantry of the PET scanner described in [3, 6], we attached the reference target onto the gantry and then used the target and the calibration tool to transform the subject's position from the POLARIS coordinate to the PET coordinate. Thus, our method allows for more flexibility in adjusting with regard to the location of the POLARIS. This is an important feature for the cardiac study due to the large inter-subject variability in the shapes of the torsos among patients, and as shown in Fig. 1e, there were enough gaps to set the best positioning for cardiac PET study. However, for exercise study, such as the studies with cycling, smaller targets and supporting post might be needed to ensure working space. An additional advantage is the portability of the POLARIS, which enables the sharing of the device among scanners in different locations.

For our technique based on the rigid body model, two targets were enough to detect the displacements and rotations of the thoraxes of the subjects, in which the secondary target was used as a reserve for cases in which the primary target was hidden from the FOV of the POLARIS. The secondary target and additional targets might be used with the corporation of the primary target to construct a non-rigid body model by detecting deformation between the chest and abdomen, and/or over the thorax region.

Another approach for the motion correction was based on image-driven information. Juslin et al. proposed an alignment technique for dynamic ^{15}O-water PET images by means of the independent component analysis. They demonstrated an improvement in quantitatively functional and parametric values, although they did not take into account for the misregistration between the transmission and emission data sets, and the movements during each emission scan [24]. The advantages of our method comparing software-based technique were (1) the misalignment between the transmission and dynamic image, and misalignment among the dynamic images could be corrected because our method was independent of the distribution and concentration of the tracer, and suboptimal image qualities (e.g., statistical noise, blurring and types of tracers). (2) Accurate attenuation correction was available because the misalignment between the transmission and the dynamic image was corrected in the reconstruction stage of the dynamic image, and (3) inherent accuracy could be obtained from the position calibration and the optical motion tracking device. Consequently, the present technique can be utilized in PET studies with several types of tracers such as ^{13}N-Ammonia and ^{18}F-FDG.

In this study, the motion correction system was demonstrated on one subject at rest. The system is to be evaluated by large population of various subjects because characteristics of motion such as magnitudes, frequencies, and directions could be different among subjects. Validation of our system is also needed for the studies during the physiologically or pharmacologically stressed conditions, in which repositioning of the heart in thoracic cavity, and larger and/or irregular (non-cyclic) chest motion by respiration would be expected. In our method, one of the limitations was correction for the misalignment due to the motion of the diaphragm with a deep breathing during a stress study, and due to the motion of the diaphragm with cough or sneezing even though during a resting study. To correct such misalignment, detection of irregular motion and a non-linear model might be needed to estimate the

location of the heart using information obtained from the locations of targets on the chest.

Our system intended to correct global movement during dynamic scans. It was expected that the system would work on transmission and emission data smoothed temporally and spatially. Attenuation correction artefacts due to respiration was out of the scope for our system, which were investigated in the X-ray combined PET system studies [25, 26].

Conclusion

Our technique using an optical motion-tracking device provided the reasonable information for correcting the global movement of the subject. It was shown that this system was applicable to detect and correct subject movement in cardiac PET studies at rest. We conclude that the present technique would contribute to improvement in the quantification of MBF in ^{15}O-water PET studies.

Acknowledgments This study was supported by a grant from New Energy and Industrial Technology Development Organization (NEDO) of Japan, the Budget for Nuclear Research of the Ministry of Education, Culture, Sports, Science and Technology (MEXT) of Japan, the Program for Promotion of Fundamental Studies in Health Science of the Organization for Pharmaceutical Safety and Research of Japan, Health Science Research Grant from the Ministry of Health, Labour and Welfare of Japan, a Grant-in-Aid for Young Scientists of the MEXT (B) (19700397) of Japan, and also a research grant for Advanced Medical Technology from the Ministry of Health, Labour and Welfare (MHLW) of Japan.

References

1. Menke M, Atkins MS, Buckley KR. Compensation methods for head motion detected during PET imaging. IEEE Trans Nucl Sci. 1996;43:310–7.
2. Picard Y, Thompson CJ. Motion correction of PET images using multiple acquisition frames. IEEE Trans Med Imaging. 1997;16:137–44.
3. Lopresti BJ, Russo A, Jones WF, Fisher T, Crouch D, Altenburger DE, et al. Implementation and performance of an optical motion tracking system for high resolution brain PET imaging. IEEE Trans Nucl Sci. 1999;46:2059–67.
4. Watabe H, Sato N, Kondoh Y, Fulton RR, Iida H. Correction of head movement using optical motion tracking system during PET study with rhesus monkey. In: Brain Imaging Using PET. San Diego: Academic Press; 2002. p. 1–8.
5. Fulton RR, Meikle SR, Eberl S, Pfeiffer J, Constable CJ. Correction for head movements in positron emission tomography using an optical motion-tracking system. IEEE Trans Nucl Sci. 2002;49:116–23.
6. Bloomfield PM, Spinks TJ, Reed J, Schnorr L, Westrip AM, Livieratos L, et al. The design and implementation of a motion correction scheme for neurological PET. Phys Med Biol. 2003;48:959–78.
7. Woo SK, Watabe H, Yong C, Kim KM, Choon C, Bloomfield PM, et al. Sinogram-based motion correction of PET images using optical motion tracking system and list-mode data acquisition. IEEE Trans Nucl Sci. 2004;51:782–8.
8. McCord ME, Bacharach SL, Bonow RO, Dilsizian V, Cuocolo A, Freedman N. Misalignment between PET transmission and emission scans: its effect on myocardial imaging. J Nucl Med. 1992;33:1209–14.
9. Germano G, Chua T, Kavanagh PB, Kiat H, Berman DS. Detection and correction of patient motion in dynamic and static myocardial SPECT using a multi-detector camera. J Nucl Med. 1993;34:1349–55.
10. Cooper JA, Neumann PH, McCandless BK. Detection of patient motion during tomographic myocardial perfusion imaging. J Nucl Med. 1993;34:1341–8.
11. Bacharach SL, Douglas MA, Carson RE, Kalkowski PJ, Freedman NM, Perrone-Filardi P, et al. Three-dimensional registration of cardiac positron emission tomography attenuation scans. J Nucl Med. 1993;34:311–21.
12. Iida H, Kanno I, Takahashi A, Miura S, Murakami M, Takahashi K, et al. Measurement of absolute myocardial blood flow with $H_2^{15}O$ and dynamic positron-emission tomography. Strategy for quantification in relation to the partial-volume effect. Circulation 1988;78:104–15 (erratum in: Circulation 1988;78:1078).
13. Iida H, Rhodes CG, de Silva R, Yamamoto Y, Araujo LI, Maseri A, et al. Myocardial tissue fraction–correction for partial volume effects and measure of tissue viability. J Nucl Med. 1991;32:2169–75.
14. Knaapen P, Boellaard R, Götte MJ, van der Weerdt AP, Visser CA, Lammertsma AA, et al. The perfusable tissue index: a marker of myocardial viability. J Nucl Cardiol. 2003;10:684–91.
15. de Silva R, Yamamoto Y, Rhodes CG, Iida H, Nihoyannopoulos P, Davies GJ, et al. Preoperative prediction of the outcome of coronary revascularization using positron emission tomography. Circulation. 1992;86:1738–42.
16. Knaapen P, Boellaard R, Götte MJ, Dijkmans PA, van Campen LM, de Cock CC, et al. Perfusable tissue index as a potential marker of fibrosis in patients with idiopathic dilated cardiomyopathy. J Nucl Med. 2004;45:1299–304.
17. Chareonthaitawee P, Kaufmann PA, Rimoldi O, Camici PG. Heterogeneity of resting and hyperemic myocardial blood flow in healthy humans. Cardiovasc Res. 2001;50:151–61.
18. Yamamoto Y, de Silva R, Rhodes CG, Araujo LI, Iida H, Rechavia E, et al. A new strategy for the assessment of viable myocardium and regional myocardial blood flow using 15O-water and dynamic positron emission tomography. Circulation. 1992;86:167–78.
19. Iida H, Rhodes CG, de Silva R, Araujo LI, Bloomfield PM, Lammertsma AA, et al. Use of the left ventricular time-activity curve as a noninvasive input function in dynamic oxygen-15-water positron emission tomography. J Nucl Med. 1992;33:1669–77.
20. Naum A, Laaksonen MS, Tuunanen H, Oikonen V, Teräs M, Kemppainen J, et al. Motion detection and correction for dynamic (15)O-water myocardial perfusion PET studies. Eur J Nucl Med Mol Imaging. 2005;32:1378–83.
21. Iida H, Miura S, Kanno I, Ogawa T, Uemura K. A new PET camera for noninvasive quantitation of physiological functional parametric images: HEADTOME-V-Dual. In: Quantification of brain function using PET. San Diego: Academic Press; 1996. 57–61.
22. Wienhard K, Dahlbom M, Eriksson L, Michel C, Bruckbauer T, Pietrzyk U, et al. The ECAT EXACT HR: performance of a new high resolution positron scanner. J Comput Assist Tomogr. 1994;18:110–8.

23. Iida H, Rhodes CG, Araujo LI, Yamamoto Y, de Silva R, Maseri A, et al. Noninvasive quantification of regional myocardial metabolic rate for oxygen by use of $^{15}O_2$ inhalation and positron emission tomography. Theory, error analysis, and application in humans. Circulation. 1996;94:792–807.
24. Juslin A, Lötjönen J, Nesterov SV, Kalliokoski K, Knuuti J, Ruotsalainen U. Alignment of 3-dimensional cardiac structures in O-15-labeled water PET emission images with mutual information. J Nucl Cardiol. 2007;1:82–91.
25. McQuaid SJ, Hutton BF. Sources of attenuation-correction artefacts in cardiac PET/CT and SPECT/CT. Eur J Nucl Med Mol Imaging. 2008;35:1117–23.
26. Gould KL, Pan T, Loghin C, Johnson NP, Guha A, Sdringola S. Frequent diagnostic errors in cardiac PET/CT due to misregistration of CT attenuation and emission PET images: a definitive analysis of causes, consequences, and corrections. J Nucl Med. 2007;48:1112–21.

Radiol Phys Technol
DOI 10.1007/s12194-008-0038-x

Use of a clinical MRI scanner for preclinical research on rats

Akihide Yamamoto · Hiroshi Sato · Jun-ichiro Enmi · Kenji Ishida · Takayuki Ose · Atsuomi Kimura · Hideaki Fujiwara · Hiroshi Watabe · Takuya Hayashi · Hidehiro Iida

Received: 27 May 2008 / Revised: 22 August 2008 / Accepted: 27 August 2008

Abstract This study evaluated the feasibility of imaging rat brains using a human whole-body 3-T magnetic resonance imaging (MRI) scanner with specially developed transmit-and-receive radiofrequency coils. The T_1- and T_2-weighted images obtained showed reasonable contrast. Acquired contrast-free time-of-flight magnetic resonance angiography images clearly showed the cortical middle cerebral artery (MCA) branches, and interhemispheric differences could be observed. Dynamic susceptibility contrast MRI at 1.17 mm^3 voxel resolution, performed three times following administration of gadolinium diethylenetriamine pentaacetic acid (Gd-DTPA, 0.1 mmol/kg), demonstrated that the arterial input function (AIF) can be obtained from the MCA region, yielding cerebral blood flow (CBF), cerebral blood volume, and mean transit time (MTT) maps. The hypothalamus (HT) to parietal cortex (Pt) CBF ratio was 45.11 ± 2.85%, and the MTT was 1.29 ± 0.40 s in the Pt region and 2.32 ± 0.17 s in the HT region. A single dose of Gd-DTPA enabled the assessment of AIF within MCA territory and of quantitative CBF in rats.

Keywords Quantitative mapping · Human whole-body 3-T MRI scanner · Single dose of Gd-DTPA · Dynamic susceptibility contrast (DSC) · Preclinical research · Rat brain

A. Yamamoto · J. Enmi · K. Ishida · T. Ose · H. Watabe · T. Hayashi · H. Iida (✉)
Department of Investigative Radiology,
Advanced Medical Engineering Center,
National Cardiovascular Center Research Institute,
5-7-1, Fujishiro-dai, Suita, Osaka 565-8565, Japan
e-mail: iida@ri.ncvc.go.jp

A. Yamamoto · A. Kimura · H. Fujiwara · H. Watabe · T. Hayashi · H. Iida
Department of Medical Physics and Engineering,
Division of Health Sciences, Graduate School of Medicine,
Osaka University, 1-7, Yamada-oka, Suita,
Osaka 565-0871, Japan

H. Sato
Laboratory for Diagnostic Solution,
Advanced Medical Engineering Center,
National Cardiovascular Center Research Institute,
5-7-1, Fujishiro-dai, Suita, Osaka 565-8565, Japan

1 Introduction

Magnetic resonance imaging (MRI) has been widely used in preclinical research on experimental small animals. Studies have typically been aimed at understanding the pathophysiologic status and evaluating the efficacy/side effects of newly developed treatments, such as pharmaceutical and regenerative medicine. Recently, a different idea has surfaced: the use of a human whole-body MRI scanner for small-animal imaging [1]. Although small-animal-dedicated scanners are superior to clinical scanners in terms of providing a better signal-to-noise ratio, the available pulse sequences are different from those in clinical scanners, and the magnetic field strength is often much higher. Small-animal imaging with clinical scanners is important for directly addressing clinical questions and/or identifying the origins of signal changes, including various disease conditions in a clinical setting.

Smith et al. [2] demonstrated that anatomic brain T_1- weighted (T_1W) images and T_2-weighted (T_2W) images can be obtained for healthy rats by using a 1-T clinical MRI scanner with a specially designed radiofrequency (RF) coil, given a reasonable spatial resolution (0.1953 × 0.1953 × 2.5 mm, 24 min of T_1W and 48 min of T_2W). The image contrast was sufficiently high to

distinguish the cortical gray matter from the white matter [corpus callosum (CC)], as well as the lateral ventricle (LV) and interpeduncular cistern (IPC) from the thalamus (Thal). Guzman et al. [3] employed a clinical 1.5-T MRI scanner with a commercially available RF coil and demonstrated that both T_1W and T_2W images can be obtained with good contrast, a reasonable spatial resolution of 0.3125 × 0.3125 × 1.5 mm, and an acquisition time of 19 min 51 s, as well as 0.35156 × 0.375 × 1.5 mm at 8 min 34 s, corresponding to T_1W and T_2W images, respectively. Other investigators [4] applied a clinical 1.5-T MRI scanner with a 3-in.-diameter circular receive-only surface coil to assess anatomic images. Their images can be used to evaluate the pathophysiologic status of stroke [4] and cancer [5, 6], as well as the effects of neural excitotoxicity [3]. There were also several studies that used a clinical 3-T MRI scanner fitted with commercial and/or hand-made RF coils to investigate the pathophysiology of stroke [7, 8] and brain tumors in rats [6, 9, 10]. Generally speaking, anatomic images with better contrast can be obtained in a stronger magnetic field, although there are additional factors that may influence the signal-to-noise ratio (SNR) or spatial resolution of anatomic images. Contrast-free time-of-flight magnetic-resonance angiography (TOF-MRA) can also be performed on rats; a reasonable spatial resolution was obtained by using a clinical 3-T MRI scanner with a single-turn solenoid coil [11].

Dynamic susceptibility contrast MRI (DSC-MRI) [12] has been widely used in clinical diagnosis, particularly in patients with stroke [13–19] and tumors [20]. The application of clinical MRI scanners has been extended to DSC-MRI studies of small animals with stroke [21, 22] and tumors [23] using a 1.5-T MRI scanner. Up to now, small-animal studies have been performed on 1.5-T MRI scanners only, and 3-T scanners have not been employed so far. This is largely attributed to the fact that the susceptibility-induced inhomogeneous magnetic field can cause more serious distortion of the images at a higher static magnetic field. In DSC-MRI studies, the echo planar imaging (EPI) technique is mainly used because fast acquisition is required for accurate tracking of the bolus passage of MR contrast agents. The EPI technique, however, is very sensitive to magnetic field inhomogeneity, and thus the EPI images of small-animal brains may be severely distorted. The gradient slew rate (SR) is not high enough to support a sufficiently short echo spacing period when clinical scanners are used for high spatial resolution imaging of small objects. Moreover, injected materials may cause further distortion [24]. The degree of distortion of dynamic EPI images of small-animal brains produced by a 3-T clinical scanner is currently unknown. The arterial input function (AIF) is also questionable. To the best of our knowledge, no DSC-MRI studies of small-animal brains on 3-T clinical scanners have been reported.

This study attempted to evaluate the feasibility of developing a human whole-body 3-T MRI system for small animals, particularly DSC-MRI with a single dose of gadolinium-diethylenetriamine pentaacetic acid (Gd-DTPA). The quality of various images—including the anatomic T_1W images, T_2W images, time-of-flight magnetic resonance angiography (TOF-MRA) images and DSC images—was tested, and the availability of the AIF obtained from rat brain was evaluated.

2 Materials and methods

2.1 Subjects

The subjects were three healthy adult rats supplied by Japan SLC, Inc. (Shizuoka, Japan). All three rats were males, and they ranged in age from 20 to 24 weeks. Their weight range was between 400 and 600 g. Anesthesia was administered with an intramuscular injection of ketamine (33 mg/kg; Daiichi-Sankyo Co., Ltd., Tokyo, Japan) and xylazine (6.6 mg/kg; Bayer Yakuhin, Ltd., Osaka, Japan). The first rat (Sprague Dawley, SD) was used for T_1-W and T_2W imaging of the whole brain. The second rat, also a SD, was used for contrast-free TOF-MRA imaging. The third was a Wistar rat, which was used for a Gd-DTPA (0.1 mmol/kg; Bayer Yakuhin, Ltd., Osaka, Japan)-enhanced DSC-MRI sequence. Experiments were carried out according to the protocol approved by the Local Committee for Laboratory Animal Welfare, National Cardiovascular Center, Osaka, Japan.

2.2 MRI acquisition

A human whole-body 3-T MRI scanner (Signa, GE Healthcare, Milwaukee, WI, USA) equipped with a 55-cm bore was employed in this study. The gradient coil system was capable of providing a maximum gradient amplitude of 40 mT/m and an SR of 150 T m^{-1} s^{-1}. All sequence programs employed in this study were designed for clinical studies.

Two solenoid coils designed for rats were specially developed to cover the whole brain, and were capable of both transmitting and receiving RF pulses. The three-turn solenoid coil, which had a diameter of 42 mm and a length along its cylindrical axis of 18 mm, was attached to an apparatus made from an acrylic mold, as shown in Fig. 1. All components of the stereotaxic apparatus consisted of nonmagnetic materials that fixed the head positions of the rats during data acquisition. The RF coil was designed to have an impedance of 50 Ω at a resonance frequency of

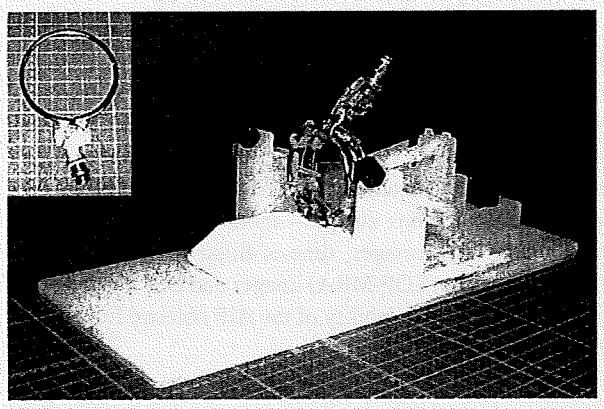

Fig. 1 The head fixation system for small animals, which was fitted with an MRI coil for RF transmission and reception. The coil is typically a three-turn solenoid; it can also be a single-turn coil, as shown on the *top left* of this figure

127.76 MHz. An additional single-turn surface coil of diameter 62 mm diameter was also developed for better homogeneity and was used for a single slice of DSC-MRI. The RF power in these coils had to be reduced to less than that used in the standard human head coil because of the diameter of the small coil. The transmission signal was therefore attenuated to 20 dB, which allowed the use of automated scanner software, including the calibration of the RF transmission power and receiver gains. All rats were fixed on the stereotaxic apparatus. They were placed at the center of the gantry and oriented with the craniocaudal axis perpendicular to the static magnetic field. Their heads were positioned inside the coil along the craniocaudal direction.

T_1W images were obtained with a conventional two-dimensional fast spin echo (2D-FSE) sequence. The repetition time (TR) was 1,500 ms [10]. The echo time (TE) was fixed at 14 ms. The echo train length (ETL) was 3. The field of view (FOV) was set at 40 × 30 mm^2, the slice thickness at 1.5 mm, the slice gap at 0.5 mm, the number of excitations (NEX) at 10, and the band width (BW) at 31.3 kHz. The acquired matrix (256 × 160) was interpolated, and null pixels were added in k-space to produce square matrices of 256 × 256. The acquisition time was 10 min 3 s.

T_2W images were obtained with a 2D-FSE and the following imaging parameters: TR, 4,100 ms; TE, 128 ms; ETL, 14; FOV, 40 × 30 mm; slice thickness, 1.5 mm; slice gap, 0.5 mm; NEX, 8; BW, 31.3 kHz; acquired matrix, 256 × 160, zero-filled to 256 × 256; phase direction, ventral-dorsal; acquisition time, 11 min 2 s.

Time-of-flight magnetic resonance angiography was performed using a three-dimensional flow-compensated spoiled gradient recalled (3D-SPGR) sequence prepared with magnetization transfer and with: TR, 53 ms; TE, 5.5 ms; flip angle (FA), 45°; BW, 16 kHz; FOV, 8 × 6 cm; slice thickness, 0.2 mm; one acquired slab of 512 × 512 × 64; voxel resolution, 0.156 × 0.156 × 0.2 mm^3; NEX, 1; acquisition time, 21 min 46 s.

Dynamic susceptibility contrast images were obtained following the intravenous administration of Gd-DTPA to the T_2*-weighted gradient echo dynamic images. A bolus of Gd-DTPA (0.1 mmol/kg) was injected manually into the tail vein with a 22-gauge catheter via 1 m of polyethylene tubing (PE50, internal diameter: 0.58 mm/outer diameter: 0.965 mm, Becton Dickinson and Company, Franklin Lakes, NJ, USA), and was followed by an additional administration of saline (1.0 ml). A multishot EPI (number of shots = 2) was employed to improve EPI distortion and temporal resolution. The imaging parameters were: TR, 142 ms; TE, 22.1 ms; FA, 20°; FOV, 40 × 40 mm; matrix size, 64 × 64, leading to a pixel size of 0.625 × 0.625 mm^2. The slice thickness was 3 mm in a single slice around the hypothalamus (HT). The temporal resolution was 0.284 s per image, and the acquisition time was 1 min 15 s. This assessment was repeated three times at intervals of 40 min and 10 min, corresponding to the first–second and second–third scans, respectively.

2.3 Data analysis

All MRI images were reconstructed on the same workstation provided for the GE Signa 3-T scanner used for the clinical programs. The images were then transferred to a Linux workstation. Lastly, data analysis was carried out using in-house and commercial software.

To evaluate the T_1W and T_2W image quality, we calculated the contrast-to-noise ratio (CNR) with an inter-tissue method [25–27] as follows: $CNR = (\pi/2)^{1/2} (SI_a - SI_b)/SI_{air}$, where SI_{air} represents the mean signal intensity of air, and SI_a and SI_b represent the signal intensities of tissue a and tissue b, respectively.

Angiograms were created by generating the partial maximum intensity projection (MIP) with commercial software [Virtual Place Liberty (VPL), AZE Co. Ltd., Tokyo, Japan]. Visible middle cerebral artery (MCA) branches and left-to-right differences in MCA were carefully investigated.

For the DSC images of slice sections containing the internal carotid artery (ICA) and/or MCA, a series of images were carefully observed. A region of interest (ROI) was carefully selected in the MCA region, from which the AIF was obtained, with the help of other anatomic information. To avoid susceptibility artifacts caused by air in the trachea, the area of the arterial circle of Willis was excluded from the definition of the AIF. The anterior cerebral artery was also excluded because of possible susceptibility effects attributed to venous blood. A Gaussian filter of full width at half maximum (FWHM) 1.1 mm

was applied to all dynamic images. The time versus signal intensity curves (TICs) were converted to the Gd-DTPA concentration according to Eq. 1 given in the "Appendix." Functional mapping images of the mean transit time (MTT), cerebral blood volume (CBV), and cerebral blood flow (CBF) were carried out with the deconvolution method [28]. The theory behind this is described in detail in the "Appendix." For ROI analysis, images of matrix size 64 × 64 were converted to 256 × 256 using a sinc interpolation function.

3 Results

T_1W and T_2W images reconstructed with a spatial resolution of 0.156 × 0.188 × 1.5 mm are shown in Fig. 2. White matter could be discriminated from cortical and deep gray matter regions. The locations of small anatomic features such as the caudate putamen (CPu), striatum, the CC, and the hippocampus (HC) could also be identified in both T_1W and T_2W anatomic images. The CNRs between the HC and CC were 15.6 and 9.8, respectively, for the T_1W and T_2W images shown in Fig. 2. The CNRs between the HC and IC were 23.2 and 13.6, respectively, although the CNR may be underestimated due to the contamination of signal from the globus pallidus.

Results for MIP images obtained with contrast-free TOF-MRA are shown in Fig. 3. Coronal MIP images around the HT of thickness 5 mm are shown in Fig. 3a. In this figure, the slice section contained ICAs and MCA. The MCA, the cortical branches in both the left and right hemispheres, can be identified. It is important to note that the anatomic structure of the cortical MCA arteries is different between the right and left hemispheres. The ROI for the AIF was selected in the MCA region and is shown by the arrows in Fig. 3a and b.

A typical example of a DSC-MRI image is shown in Fig. 4. Distortion of the DSC-MRI images is visible in Fig. 4A in the phase direction. A magnified area from dynamic images of the MCA region (shown as a rectangle in Fig. 4A) is displayed in Fig. 4B. Several pixels indicate temporal changes in pixel contrast as a function of time, and these are reflected by Gd-DTPA negative enhancement. The pixel signal intensity varied as shown in Fig. 4C, and the curve shown was employed to estimate the AIF. Figure 5 shows the TIC in this area together with the TIC for the whole brain region obtained from each of the three scans. The curves were visually reproducible in terms of the shapes, heights and widths of the curves around the peak, as well as the tail height at the end of the scan. It should also be noted that the baseline was consistent before each injection of Gd-DTPA, even though the second and

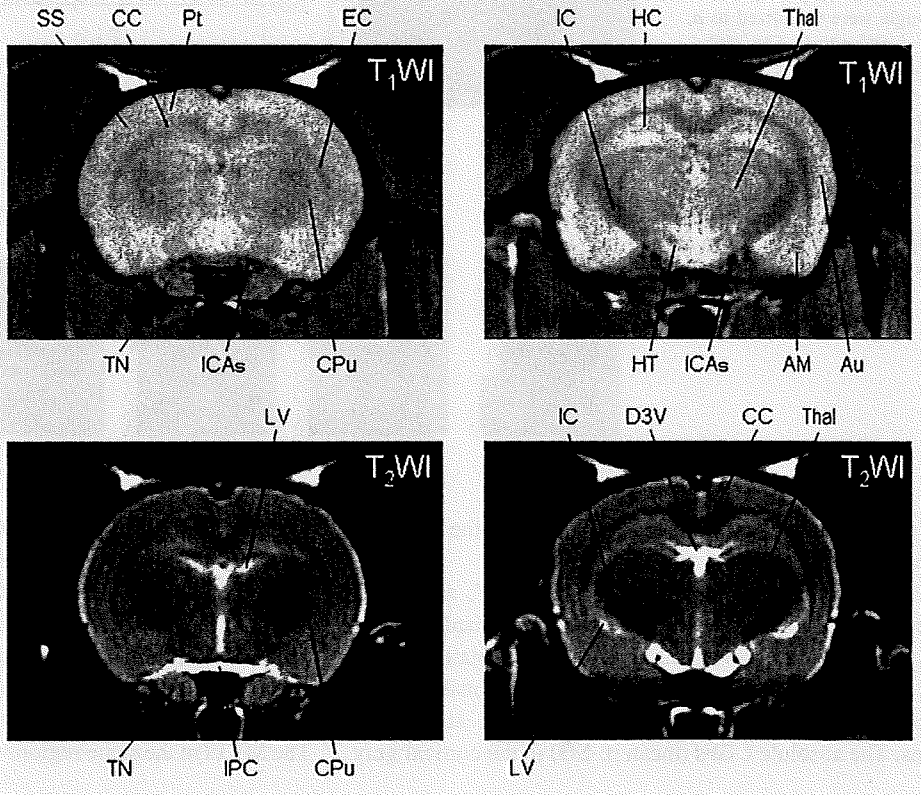

Fig. 2 T_1W images (*top*) and T_2W images (*bottom*) obtained from an SD rat, with the following anatomic locations as indicated: the somatosensory cortex (*SS*), corpus callosum (*CC*), parietal cortex (*Pt*), external capsule (*EC*), caudate putamen (*CPu*), internal capsule (*IC*), hippocampus (*HC*), thalamus (*Thal*), auditory cortex (*Au*), amygdala (*AM*), hypothalamus (*HT*), internal carotid arterial system (*ICAs*), trigeminal nerve (*TN*), interpeduncular cistern (*IPC*), dorsal third ventricle (*D3V*), and the lateral ventricle (*LV*). These slice sections were located −1.5 mm (*left*) and −3.5 mm (*right*), respectively, from the bregma

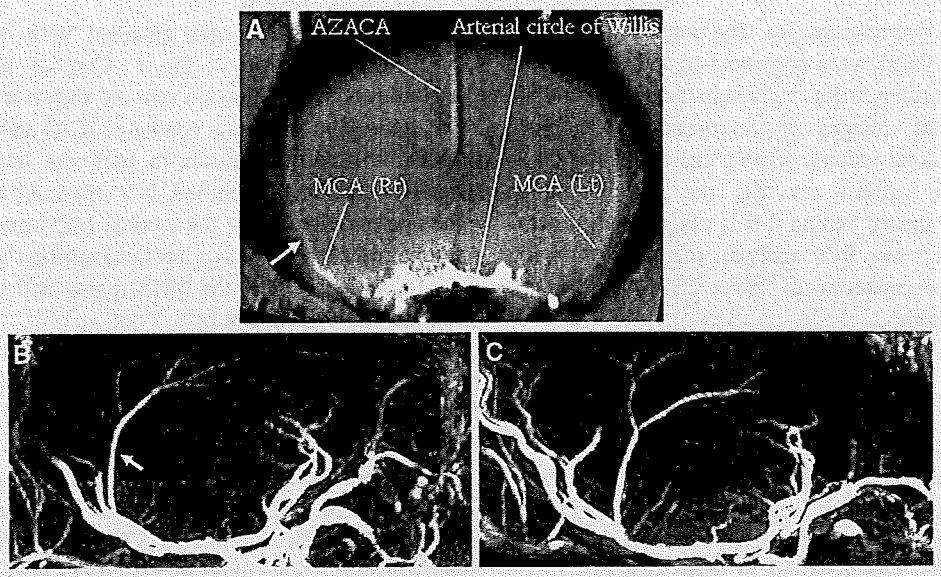

Fig. 3 Partial maximum intensity projection maps of contrast-free time-of-flight MRA obtained for a Sprague Dawley rat. Maps represent areas around the Thal (**a**), right hemisphere (**b**), and left hemisphere (**c**). The *white arrows* indicate the selected ROI level (as described in the "Discussion"). *AZACA*, azygos anterior cerebral artery

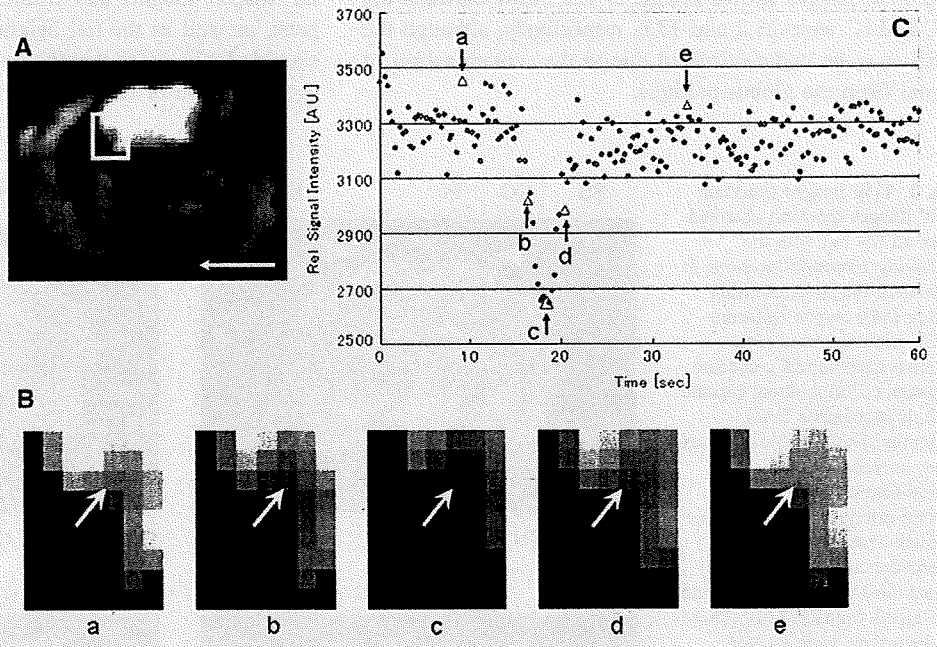

Fig. 4 Typical time-frame images obtained from Gd-bolus tracking T_2*-weighted dynamic images (after the first injection). A *white rectangle* was placed in the MCA area (**a**), and magnified images of this rectangle were visualized as *a*, *b*, *c*, *d*, and *e* in **b**. The TIC within the pixels is indicated by *white arrows* in **b**. The data were then plotted in a graph (**c**). Typical data points were extracted from the first injection at the times of 9.2 (*a*), 16.4 (*b*), 18.1 (*c*), 20.1 (*d*), and 33.9 (*e*) s. The phase direction is shown as a *white arrow* in **a**

the third curves should have been affected by the previous injection of Gd-DTPA.

Functional mapping images of CBF, CBV, and MTT calculated according to the theory described in the "Appendix" are shown in Fig. 6. Images obtained from this sequential assessment appeared to be reasonably clear, although slightly noisy, and were consistent among the scans. The absolute CBFs (mean ± SD) in the cortical gray matter area (mainly the parietal cortex, Pt) were 24.04 ± 2.88, 17.75 ± 3.34, and 31.87 ± 7.27 ml g^{-1} min^{-1} for the first, second, and third scans, respectively. The HT-to-Pt CBF ratios were 46.7, 51.5, and 43.0% for the first, second, and third scans, respectively. The CBVs were 0.49 (0.44), 0.50 (0.35), and 0.47 (0.41) ml/ml in the Pt (the HT) region in the first, second, and third scans, respectively. The MTTs in the same regions were 1.22 (2.51), 1.72 (2.29),

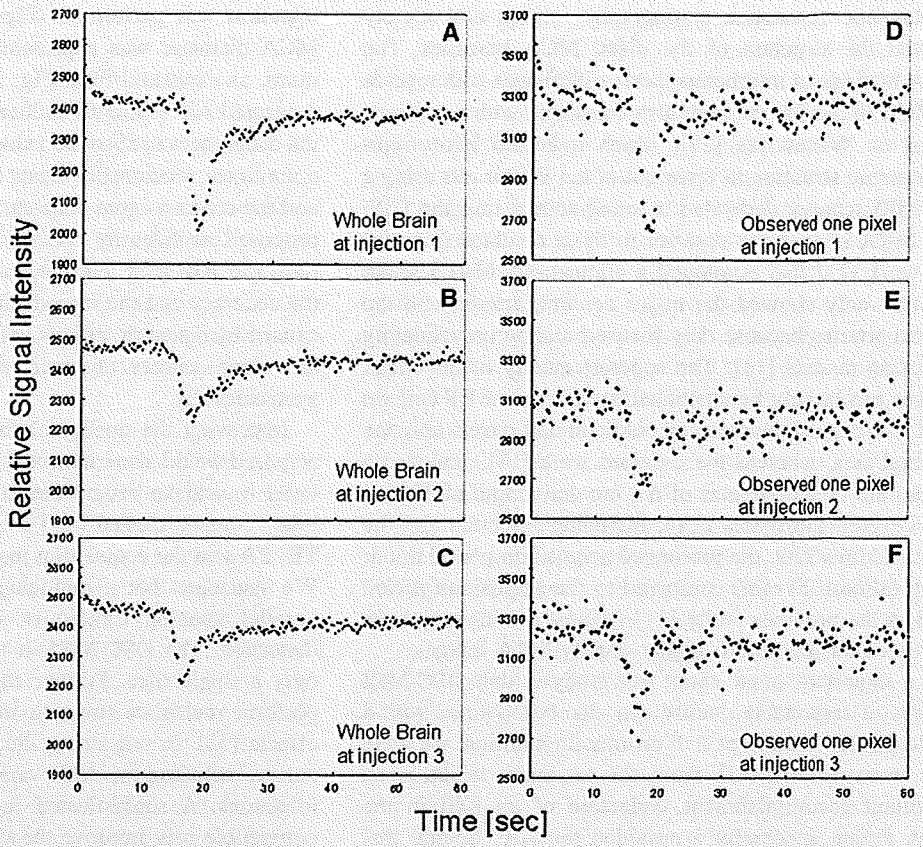

Fig. 5 TIC dynamic changes in the whole brain are shown in the first injection (**a**), the second injection (**b**), and the third injection (**c**). For each injection, a one-pixel ROI was selected and observed, as shown for the first (**d**), second (**e**) and third (**f**) injections, respectively. The negative enhancement changes in the rate from peak signal intensity to baseline were 16.8% (**a**), 10.0% (**b**), and 10.3% (**c**) at the whole brain (average 12.3, SD 3.9). The peak-to-base fractions at selected ROIs were 19.2% (**d**), 14.5% (**e**), and 16.9% (**f**) (average 16.9, SD 2.3), for the first, second, and third injections, respectively

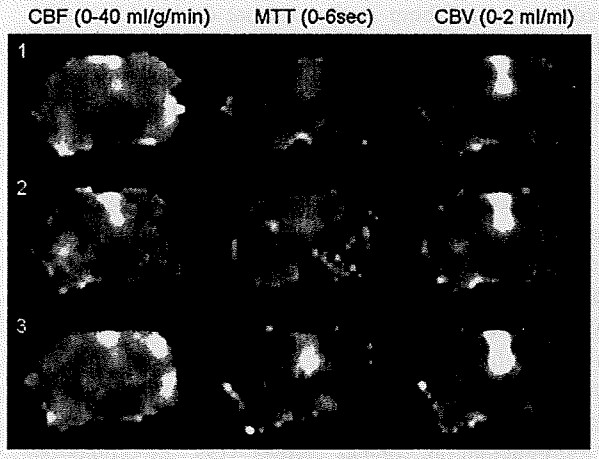

Fig. 6 *First column on the left*: CBF maps using the AIF from MCA, pictured in a grayscale from 0 to 4 ml g^{-1} min^{-1}. MTT maps are shown in the *middle column*, followed by CBV maps of 0–2 ml g^{-1} min^{-1} in the *column on the right*. Deconvolution was carried out pixel by pixel with b-SVD and then smoothed to 0.15625 × 0.15625 mm in-plane resolution from the acquired voxel resolution of 0.625 × 0.625 × 3 mm (1.17 mm^3) in DSC-MRI

and 0.92 (2.16) s in each of the three scans. Among the three injections, the absolute MTTs (mean ± SD) were 1.29 ± 0.40 s in the Pt and 2.32 ± 0.17 s in the HT region.

4 Discussion

This study demonstrated that our system of a human whole-body 3-T MRI fitted with an in-house solenoid coil developed for small animals can provide morphologic and functional images of the rat brain in vivo. The quality of T_1W and T_2W images obtained with a scan duration of approximately 10 min was better than those obtained in previous studies in which 1.5-T clinical MRI scanners [3] were employed. The neocortex and large subcortical structures, such as the Thal and HC, are readily recognized from their topographic relationship to the CC, the ventricular system, and the subarachnoid space [2]. In T_1W images, the cerebrospinal fluid (CSF)-containing spaces are visible as they are hypointense, and the arterial flow showed a signal loss caused by so-called flow void effects, which is typically seen in the spin echo sequence [2]. In T_2W images, the CSF was bright and white (prolonged T_2 relaxation time), whereas the myelinated white matter was black (short T_2 relaxation time). The white matter tracts such as the IC and CC were clearly visible in both T_1W and T_2W images, and better quality was obtained compared to previous reports employing 1.0- and 1.5-T clinical MRI scanners [2, 3].

Magnetic resonance angiography images also clearly showed the structure of the distal MCA branches. The MRA findings of interhemispheric differences with regards to MCA in the SD rat were also consistent with a previous report on Wistar rats [29], which indicated left-to-right asymmetric structure in three out of ten Wistar rats using a 7-T MRI scanner dedicated to small-animal imaging [29]. Our MRA images are superior to those obtained in previous work [11] that employed a clinical 3-T MRI scanner and that only showed the major cerebral arteries and the carotid arteries because they focused mainly on validating occlusion models [11]. The superior quality of our MRA images can largely be attributed to the type of RF coil we used. Ours is a three-turn solenoid coil that covers only the cerebral area, whereas the previous work [11] employed a single-turn coil (diameter of 6.4 cm and length of 10 cm) that covered the whole head, including the brain and the neck. Additionally, the prolonged acquisition period in our study (almost 20 min) compared to the acquisition period used in the previous study [11] (almost 4 min) may have been a factor that led to higher-quality MRA images.

An important point about this study is that DSC-MRI images of reasonable quality can also be obtained with a clinical MRI scanner at 3 T on rats. In addition, we were able to extract the AIF from the rat brain, which is an important accomplishment. Selection of an ROI in the MCA region successfully provided the AIF. Spatial distortion or susceptibility artifacts were not visible in our observations. Signal changes were obtained during DSC-MRI following a single dose of Gd-DTPA. During this study, the dedicated transmit and receive RF coils were considered to be crucial to obtaining a reasonable SNR. Our study was performed with the same sequence and the same dose rate (0.1 mmol/kg) of Gd-DTPA that are commonly used in clinical examinations. Moreover, it was performed with high (1.17 mm^3)-resolution dynamic imaging.

The quantitative images of CBF were consistent with those in a previous report on the use of [^{14}C] iodoantipyrine [30]. Namely, the HT-to-Pt contrast in CBF was 43–52% in this study, which is close to the values reported by Bloom et al. [30] of 44–58%. Although the absolute CBF and CBV values in our study were different from those obtained previously [13, 30, 31], the uncertain scaling factors for each of these were canceled out when calculating the MTT with Eq. 5 [32] (see also the "Appendix"). The MTT obtained in this study was comparable to those obtained in previous work [31, 33].

We noticed that the absolute CBF and CBV values were overestimated, which suggests that some limitations apply, such as the partial volume effect (PVE) caused by insufficient spatial resolution as compared with the anatomic structure of the MCA. Detection of AIF with a repeat injection was performed (Fig. 5, right row). The major MCA diameter was approximately 0.5 mm at the maximum, as evaluated from Fig. 3, which suggested that the measured AIF is largely influenced by the PVE [24]. Also, the differences in absolute value may be due to the fact that a nonlinear relationship exists between the signal intensity and the contrast agent concentration. Previous reports have proposed nonlinearity correction methods for brain tissue [34] and AIF [35]. Further studies are needed to confirm the accuracy and the reproducibility [36]. Image distortion caused by dielectric effects [37] and/or EPI distortion [38] are other sources of error, and should be investigated systematically.

Improving the quality of the original dynamic images acquired would also improve the mapping image quality. In order to achieve better detection of the dynamic susceptibility contrast caused by T_2* signals, the optimization of TE, FA and the acquisition matrix should be investigated. We speculate that a multichannel phased array coil and parallel imaging techniques would reduce the level of distortion. The DSC-MRI in this study was obtained for only a single slice. Further careful attention is needed to perform multislice imaging in order to minimize inflow effects [35]. In our study, the contrast concentration $C(t)$ curves including the AIFs varied slightly among the three injections. A sophisticated injector system that is MR-compatible may improve the variation.

A dedicated high magnetic field scanner equipped with a dedicated small bore is the optimal device for small-animal imaging. However, such systems are not commonly available. The system developed in this study might serve as a low-cost solution or an alternative. The use of the present system provides an opportunity to use the same imaging platform available for clinical studies for small-animal imaging [7]. This would allow us to determine pathophysiological status from MRI signals using animal models with various diseases. More importantly, the optimization of several scan parameters, which has been difficult to achieve in clinical patients, can easily be performed on small animals with this system. In particular, the reproducibility of the assessment of CBF with DSC-MRI, which has been reported to be a limitation on clinical studies [19, 36], could be improved by performing a systematic evaluation of each scan parameter when this system is used on small animals rather than clinical patients. With the addition of a high-strength insert gradient coil [39], which allows for thinner slices and much faster read-out, the system performance and the spatial resolution with an acceptable SNR can be improved. The use of adapting coils could be an effective solution for those who operate MR scanners for human subjects and intend to gain experience [40] in preclinical research.

5 Conclusion

In this preclinical study on rats, reasonable image quality was obtained for T_1W, T_2W, and contrast-free TOF-MRA images generated using a human whole-body 3-T MRI scanner and a newly developed solenoid coil. In DSC-MRI, this system visualized transient signal changes with a single dose of Gd-DTPA and using the same sequences commonly used in clinical examinations. A human whole-body 3-T MRI scanner and dedicated coil make it possible to detect the AIF in the MCA region of Wistar rats. High-resolution DSC-MRI was accomplished with a clinical scanner, but the spatial resolution with an acceptable SNR was insufficient for the rat brain. Although there may be some remaining issues relating to AIF, we have shown the potential of DSC-MRI in our study.

Acknowledgments The authors would like to express our appreciation to the reviewers, the editors and the editorial assistants of *Radiological Physics and Technology* for their invaluable advice on how to improve our manuscript. This study was supported by a grant for research on Advanced Medical Technology from the Ministry of Health, Labor and Welfare, Japan. We would like to thank the VPL released by AZE Ltd. (Tokyo, Japan) and the software library provided by the Oxford University Center for Functional MRI of the Brain. We are grateful to the staff at the National Cardiovascular Center for their invaluable contributions and efforts. Last but not least, we would like to express our thanks to Miss Atra Ardekani (a summer intern from McGill University in Montreal, Quebec, Canada).

Appendix: Calculation of functional mapping images from DSC-MRI

The observed TIC $S(t)$ was converted to a time-versus-concentration curve (TCC) $C(t)$ by the following equation [16, 36]:

$$C(t) = k \cdot \Delta R2^*(t) = -k \cdot \ln(S(0)/S(t))/\mathrm{TE}, \quad (1)$$

where $\Delta R2^*$ is the change in the T_2^* relaxation rate and k is a constant. In this study, it was assumed that $k = 1$. $S(0)$ is the pre-contrast (baseline) signal and $S(t)$ is the measured signal at time t. The next step was to fit this first-pass period of TCC to a gamma variate function:

$$C(t) = a(t-b)^c \exp(-(t-b)/d), \quad (2)$$

where a, b, c, and d were determined by nonlinear least-squares fitting. To minimize the effects of the recirculation of the contrast agent, data were neglected in the fit if these concentrations were less than 50% of the maximum after the peak of the TCC.

The fitted tissue TCC $Ct(t)$ was deconvolved by the fitted AIF $C_{\mathrm{AIF}}(t)$ by using singular value decomposition with a block-circulant deconvolution matrix (b-SVD) method [28] according to the equation

$$\mathrm{CBF} \cdot R(t) = Ct(t) \otimes^{-1} C_{\mathrm{AIF}}(t), \quad (3)$$

where $\otimes^{-1}$ represents the deconvolution operator and $R(t)$ is a residue function representing the tissue response to an instantaneous bolus. $\mathrm{CBF} \cdot R(t)$ was estimated by deconvolving $Ct(t)$ by $C_{\mathrm{AIF}}(t)$ using b-SVD, and then CBF was determined as the maximum value of the obtained $\mathrm{CBF} \cdot R(t)$.

The CBV was calculated as follows:

$$\mathrm{CBV} = \int_0^\infty Ct(t)\mathrm{d}t \Big/ \int_0^\infty C_{\mathrm{AIF}}(t)\mathrm{d}t. \quad (4)$$

Lastly, the MTT is calculated from CBF and CBV by applying the central volume principle [32]:

$$\mathrm{MTT} = \mathrm{CBV}/\mathrm{CBF}. \quad (5)$$

References

1. Brockmann MA, Kemmling A, Groden C. Current issues and perspectives in small rodent magnetic resonance imaging using clinical MRI scanners. Methods. 2007;43:79–87.
2. Smith DA, Clarke LP, Fiedler JA, Murtagh FR, Bonaroti EA, Sengstock GJ, et al. Use of a clinical MR scanner for imaging the rat brain. Brain Res Bull. 1993;31(1–2):115–20.
3. Guzman R, Lövblad KO, Meyer M, Spenger C, Schroth G, Widmer HR. Imaging the rat brain on a 1.5 T clinical MR-scanner. J Neurosci Methods. 2000;97(1):77–85.
4. Fujioka M, Taoka T, Matsuo Y, Hiramatsu KI, Sakaki T. Novel brain ischemic change on MRI: delayed ischemic hyperintensity on T_1-weighted images and selective neuronal death in the caudoputamen of rats after brief focal ischemia. Stroke. 1999;30(5):1043–6.
5. Thorsen F, Ersland L, Nordli H, Enger PO, Huszthy PC, Lundervold A, et al. Imaging of experimental rat gliomas using a clinical MR scanner. J Neurooncol. 2003;63(3):225–31.
6. Biswas J, Nelson CB, Runge VM, Wintersperger BJ, Baumann SS, Jackson CB, et al. Brain tumor enhancement in magnetic resonance iimaging: comparison of signal-to-noise ratio (SNR) and contrast-to-noise ratio (CNR) at 1.5 versus 3 Tesla. Invest Radiol. 2005;40:792–7.
7. Shimamura M, Sato N, Sata M, Kurinami H, Takeuchi D, Wakayama K, et al. Delayed postischemic treatment with fluvastatin improved cognitive impairment after stroke in rats. Stroke. 2007;38:3251–8.
8. Lee JM, Zhai G, Liu Q, Gonzales ER, Yin K, Yan P, et al. Vascular permeability precedes spontaneous intracerebral hemorrhage in stroke-prone spontaneously hypertensive rats. Stroke. 2007;38:3289–91.
9. Wintersperger BJ, Runge VM, Biswas J, Reiser MF, Schoenberg SO. Brain tumor enhancement in mr imaging at 3 Tesla: comparison of SNR and CNR gain using TSE and GRE techniques. Invest Radiol. 2007;42:558–63.
10. Sato H, Enmi J, Teramoto N, Hayashi T, Yamamoto A, Tsuji T, et al. Comparison of Gd-DTPA-induced signal enhancements in rat brain C6 glioma among different pulse sequences in 3-Tesla magnetic resonance imaging. Acta Radiol. 2008;49:172–9.
11. Yang YM, Feng X, Yao ZW, Tang WJ, Liu HQ, Zhang L. Magnetic resonance angiography of carotid and cerebral arterial